# Sustaining mechanism of small-scale turbulent eddies in a precessing sphere

Yasufumi Horimoto* and Susumu Goto†
*Graduate School of Engineering Science, Osaka University, 1-3 Machikaneyama, Toyonaka, Osaka, 560-8531 Japan*
(Received 23 March 2017; published 10 November 2017)

It has been known for a long time that fully developed turbulence is sustained in a precessing container. The aim of the present study is to reveal the sustaining mechanism of turbulence in a precessing sphere by means of laboratory experiments. We conduct experiments using a Newtonian fluid (water) and viscoelastic fluids (dilute solutions of surfactant, cetyltrimethyl ammonium chloride, and polymers, polyethylene oxide) to understand the sustaining mechanism of turbulence of Newtonian fluids by examining turbulence modifications due to the surfactant and polymer additives. When the Reynolds number based on the spin angular velocity and radius of the sphere is fixed, the most developed turbulence is sustained with the Poincaré number (the precession rate) being about 0.1. The key ingredient of the developed turbulence is a pair of large-scale vortex tubes which robustly exists in the flow. Assuming that these vortex tubes sustain small-scale turbulent eddies through an energy cascading process, we can explain all our experimental observations. Concerning the turbulence modification by the additives, the time-scale criteria by Lumley [J. Polymer Sci.: Macromol. Rev. **7**, 263 (1973)] and the refined theory by Tabor and de Gennes [Europhys. Lett. **2**, 519 (1986)] explain the experimental result that the pair of large-scale vortex tubes survives even when small-scale turbulent eddies are drastically suppressed by the surfactant additive.

DOI: 10.1103/PhysRevFluids.2.114603

## I. INTRODUCTION

Since table-top turbulence generators are useful for scientific and engineering studies of turbulence, it is important to establish an efficient way to generate turbulent flows of a fluid confined in a container. The simplest way to sustain turbulence of a confined fluid is to mix it with inserted stirrers. For instance, the von Kármán flow [1,2], which is driven by a pair of counter-rotating disks in a columnar container, is widely used. The Taylor-Couette flow [3], i.e., the flow between rotating concentric columns, is an example of flow systems sustaining complex flows without stirrers and is extensively used in laboratory experiments of turbulence (for a recent review see Ref. [4]). Another method to sustain turbulence of a confined fluid without stirrers is using the precession of a container [5,6]. A precession is the rotation of the spin axis of a rotating container about another axis (see Fig. 1). In the present study, we focus on the fact that weak precession of a container can sustain developed turbulence of the confined fluid.

Since the pioneering experiment by Malkus [5], many researchers have studied the flows in precessing containers with various shapes: a cylinder [7–18], a spheroid [18–27], a sphere [28–39], and spheroidal or spherical shells [40–46]. In particular, geophysicists are interested in this flow system because the Earth's weak precession may affect the geomagnetic dynamo due to turbulence of molten iron in the outer core [5,47–49]. This is the reason why flows in a precessing spheroid and a spheroidal shell have been extensively studied. However, as shown in Ref. [50], turbulence is sustained in a sphere with much weaker precession than a slightly elongated spheroid. Therefore, in the present study, we investigate turbulence in a spherical cavity. Once we fix the angle between the

*y_horimoto@fm.me.es.osaka-u.ac.jp
†goto@me.es.osaka-u.ac.jp

 

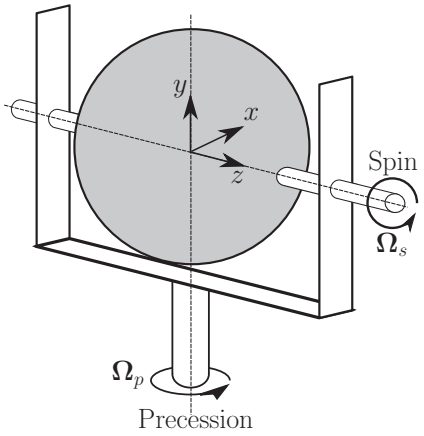


FIG. 1. Precessing sphere. We examine the case that the axes of the spin and precession are perpendicular to each other. Here $\mathbf{\Omega}_s$ and $\mathbf{\Omega}_p$ denote the spin and precession angular velocities, respectively.

two rotational axes (see Fig. 1), the flow of a Newtonian fluid in a precessing sphere is controlled by only two dimensionless parameters (see Sec. II A). This is an advantage of this system. Recall that the von Kármán flow and the Taylor-Couette flow have additional parameters such as the aspect ratio and the shape of disks. We also emphasize that one may conduct direct numerical simulations (DNSs) [38,39,51] of flows in a precessing sphere at the Reynolds numbers as high as in laboratory experiments because of its simple boundary condition.

One of the most interesting properties of this system is that the precession of a spherical container drives a variety of flows in spite of its simple motion. In our previous experiments [6,50], we systematically investigated from steady flows to developed turbulence in a precessing sphere and showed that the most developed turbulence (for a given spin rate) is sustained when the precession is only about 10% of the spin. This property is independent of the spin rate. We also quantitatively showed, using DNSs [51], that only 10–15 spins are required to completely mix a Newtonian fluid (irrespective of its kinematic viscosity) confined in a precessing sphere when the precession rate is set around 10%. According to our DNSs, a pair of large vortex tubes exists in this strongly mixing regime. Figure 2 shows these vortices, which are depicted with streamlines of the temporally

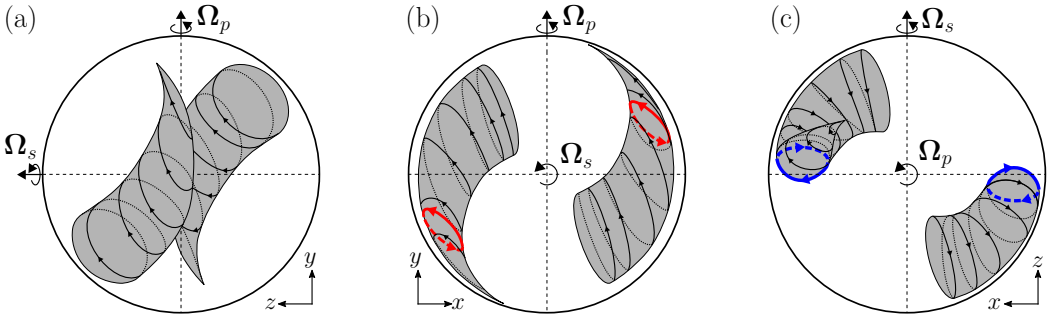


FIG. 2. Schematics of a pair of large-scale vortex tubes in turbulence of a Newtonian fluid for Po = 0.1. (Here Po indicates the precession rate; see Sec. II A for the definition.) These are depicted on the basis of DNSs [50,51]. Black arrows are streamlines of the averaged velocity field of turbulence. Red and blue curves show the cross-sectional flows on the $x$-$y$ and $z$-$x$ planes, respectively. The vortices are anticyclones with angular velocities approximately antiparallel to $\mathbf{\Omega}_p$.

averaged velocity field [50,51]. They are anticyclonic with respect to the angular velocity of the precession [see the blue curves in Fig. 2(c)] and the helical streamlines in the left (right) vortex in Fig. 2(b) are right- (left-)handed. Although we speculate that the large-scale vortex tubes play important roles in the sustaining mechanism of small-scale turbulent eddies, the detailed mechanism is unknown. The main purpose of the present study is to show how the developed turbulence is sustained with a precession as weak as 10% of the spin.

Despite the long history, back to the time of Poincaré, of the theoretical study of flows in precessing containers, the sustaining mechanism of turbulence in a precessing sphere or spheroid is not understood. In the same year of Malkus's experiment [5], Busse [21] developed the theory of flows in a precessing spheroid in the weak precession regime. He extended the linear boundary-layer analysis by Stewartson and Roberts [19] and Roberts and Stewartson [20] to the nonlinear regime, and he derived viscous corrections to the inviscid steady flow solution. Concerning the instability, Kerswell [25] showed that the parametric coupling of two inertial waves in a precessing spheroid could lead to unsteady flow through an inviscid instability. Kida [34,35] analytically investigated the viscous steady flow in a weakly precessing sphere and its instability, and derived the scaling of the critical precession rate as a function of the Reynolds number, which is in agreement with the laboratory experiments [50]. Even recently, Lin *et al.* [38] analytically and numerically investigated the mechanism and scaling of the instability of steady flow in a weakly precessing sphere, where the differential rotation between the container and confined fluid plays an important role because, as the Poincaré number increases, the differential rotation grows, and then the growth rate of the linear instability increases accordingly. Although these stability analyses explain the onset of unsteady flows in a weak precession regime, they provide no information on the sustaining mechanism of fully developed turbulence. We tackle this problem by conducting laboratory experiments.

In the present study, to understand the sustaining mechanism of fully developed turbulence of a Newtonian fluid confined in a precessing sphere, we investigate flows of non-Newtonian fluids in the sphere. It is well known that a small amount of additives can significantly modify turbulence of water due to the viscoelastic properties of the solutions [52–55]. The most famous phenomenon may be known as the Toms effect [56], namely, the addition of a small amount of some kind of polymers significantly reduces turbulence intensity. By systematically investigating the turbulence reduction due to additives, we may reveal the sustaining mechanism of turbulence of Newtonian fluids because the turbulence reduction must be caused by the inhibition of the sustaining mechanism of the turbulence.

For this purpose, we must know rheological properties of the solutions of additives which lead to the turbulence reduction. Fortunately, since the discovery of the Toms effect, for engineering applications such as the drag reduction in fluid transports, not only the rheological properties of the solutions but also the physical mechanism of the reduction have been investigated by many authors [52–55]. In our experiments, we use dilute solutions of surfactant and polymer additives whose rheological properties are known (see Sec. II C). Concerning the physical mechanism of turbulence modification, we will discuss it in Sec. IV on the basis of classical theories [57–60] which predict the truncation of the energy cascade at a length scale. In the following, this length scale is denoted by $\ell_c$. The starting point of these theories is the time-scale criteria: i.e., the matching of time scales of turbulent energy cascade and the viscoelasticity of the working fluid. We define the Lumley scale (denoted by $\ell_L$) by the length scale at which the time scale of shearing motions around eddies is comparable to the characteristic time (denoted by $\tau$) of the viscoelasticity. Below the Lumley scale, the flow can interact with the additive. According to Tabor and de Gennes [59] (see also a recent review [54]), at $\ell_c$, which is shorter than $\ell_L$ and depends on the concentration of the additive, the elastic energy possessed by the additive is comparable to the energy possessed by turbulent eddies and the energy cascade is terminated so that eddies smaller than $\ell_c$ are not sustained. Note that these classical theories have been developed for polymer solutions, but surfactant additives have similar effects.

The rest of the present article is organized as follows. After describing our experimental setup in Sec. II, we show in Sec. III experimental results on the turbulence reduction in a precessing sphere

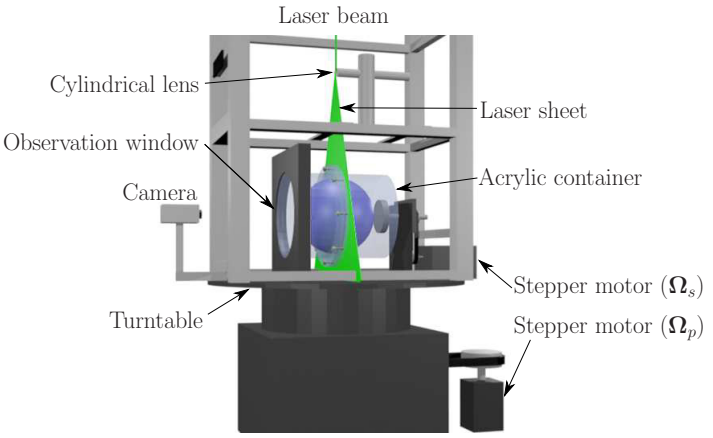


FIG. 3. Experimental apparatus. Two stepper motors drive the spin and precession of the acrylic container. A laser sheet visualizes the flow on the equatorial plane of the spherical container. A camera fixed on the turntable records visualized flows through the observation window at the bottom of the container. It is mounted on a linear stage to record flows at different locations on the equatorial plane.

due to surfactant and polymer additives. In Sec. IV we use classical theories [57–60] to explain our experimental results for non-Newtonian fluids and reveal the sustaining mechanism of turbulence of Newtonian fluids in a precessing sphere. Section V gives concluding remarks.

## II. EXPERIMENTS

### A. Experimental apparatus

We experimentally investigate turbulence of an incompressible fluid in a precessing sphere with radius $a$ (=90 mm). The sphere rotates at a constant angular velocity, $\mathbf{\Omega}_s$, and its spin axis rotates at a constant angular velocity, $\mathbf{\Omega}_p$, about another axis that is called the precession axis (Fig. 1). In our experiments, the axes of the spin and precession are set at a right angle. We define $x$, $y$, and $z$ axes in the directions parallel to $\mathbf{\Omega}_p \times \mathbf{\Omega}_s$, $\mathbf{\Omega}_p$, and $\mathbf{\Omega}_s$, respectively. When the working fluid is Newtonian with the kinematic viscosity, $\nu$, the flow in the precessing sphere is controlled by two dimensionless parameters: the Reynolds number, $\mathrm{Re} = a^2\Omega_s/\nu$, and the Poincaré number, $\mathrm{Po} = \Omega_p/\Omega_s$. Here $\Omega_s = |\mathbf{\Omega}_s|$ and $\Omega_p = |\mathbf{\Omega}_p|$.

The schematic of our experimental apparatus is shown in Fig. 3. We use a columnar acrylic container with a spherical cavity. To realize the precession of the container, we drive the spin of the container at $\mathbf{\Omega}_s$ by using a stepper motor (with a step angle 0.036°) on a table which is also rotated at $\mathbf{\Omega}_p$ by another stepper motor (with a step angle 0.072°). Since the turntable and the container are independently rotated by the two motors, we can precisely set the values of Re and Po.

There are heat sources such as the motors and a computer around the acrylic container. Since the temperature of the working fluid affects the rheological properties, including the kinematic viscosity, $\nu$, of solutions of surfactant and polymer additives, keeping the temperature of the working fluid constant is crucial to conduct experiments with high reproducibility. We embed a thermister in the acrylic container to monitor the temperature of the working fluid. To precisely control the temperature of the fluid, we enclose the space of about 2 $\mathrm{m}^3$ around the experimental apparatus with thermal insulators and control the air temperature by using a well-controlled air conditioner (Orion Machinery PAP 03B). We can thus keep the temperature of the fluid at $20.0 \pm 0.1\,^{\circ}\mathrm{C}$ during the experiments for over 10 hr.

TABLE I. Examined Reynolds numbers, Re, and the corresponding values of the magnitude of the spin angular velocity, $\Omega_s$.

| Re | $1.01 \times 10^4$ | $2.03 \times 10^4$ | $4.01 \times 10^4$ | $8.02 \times 10^4$ |
|---|---|---|---|---|
| $\Omega_s$ [rad/s] | $0.4\pi$ | $0.8\pi$ | $1.58\pi$ | $3.16\pi$ |

### B. Visualizations and PIV

We conduct flow visualizations using reflective flakes and velocity measurements by particle image velocimetry (PIV). The light source is common for these two kinds of experiments. The laser beam with the wavelength 532 nm and the maximum power 2 W, which is emitted from a laser oscillator fixed in the room, is led to the turntable along its rotation axis (i.e. the precession axis). The laser beam, then, is spread into a sheet by a cylindrical lens fixed on the turntable to visualize the flow on the equatorial plane of the spherical cavity, that is the $x$-$y$ plane at $z = 0$ (Fig. 3). The refraction in the $z$ direction of the incident laser sheet at the outer wall of the container is negligible because the sheet enters through the side surface of the columnar container. We make flow visualizations and velocity measurements through the flat bottom window of the columnar container. Although the indices of the acrylic container and working fluids (Sec. II C) are different by about 11%, the refraction on the spherical cavity is negligibly small.

We use two different cameras for flow visualizations and PIV. We use a digital camera (Nikon D7100 with Nikkor 20 mm 1:2.8; $1280 \times 720$ pixels) fixed on the turntable to record visualized flow on the equatorial plane, whereas we use another digital camera (Ditect HAS-220 with Pentax C-mount lens 12 mm 1:1.2; $640 \times 480$ pixels) for PIV. In the present study, we conduct experiments for $\mathrm{Re} = 1.01 \times 10^4$, $2.03 \times 10^4$, $4.01 \times 10^4$, and $8.02 \times 10^4$. The corresponding values of $\Omega_s$ to each Reynolds number are summarized in Table I. For flow visualizations, we fix the frame rate at 50 fps. For PIV, we set the frame rates at 50 fps for $\mathrm{Re} = 1.01 \times 10^4$, 100 fps for $\mathrm{Re} = 2.03 \times 10^4$ and $4.01 \times 10^4$, and 200 fps for $\mathrm{Re} = 8.02 \times 10^4$.

Due to the limitation of the resolution of the digital camera, we set the camera on a linear stage to conduct the PIV at three different locations in the $x$ direction for each parameter so that we can obtain the velocity field in the semicircle region ($y \gtrsim 0$) on the equatorial plane. Assuming the rotational symmetry about the spin axis of the statistics of the velocity on the plane, we may obtain the statistics on the entire plane. We collect statistics over about 280 $T_s$ for $\mathrm{Re} = 1.01 \times 10^4$ and $2.03 \times 10^4$, and 140 $T_s$ for $\mathrm{Re} = 4.01 \times 10^4$ and $8.02 \times 10^4$. Here $T_s$ is the spin period.

We emphasize that our PIV measures the velocity field in the rotating frame fixed on the turntable and that we do not subtract any rotating components, the spin rotation of the container, for example, from the measured velocity field (see Figs. 7 and 9). For a lower Poincaré number, turbulent flow globally rotates about an axis inclined from the spin axis of the container (see the Appendix for the case $\mathrm{Po} = 0.02$), and there are coherent large vortices rotating with the global circulation [38,39]. However, there is no primary rotation in fully developed turbulence for $\mathrm{Po} = 0.1$ (see Fig. 2), which is the main target of the present study.

We use different tracer particles for flow visualizations and PIV measurements. For flow visualizations, we use aluminum reflective flakes or mica coated with titanium dioxide. No qualitative difference in the visualizations with the two kinds of reflective flakes is observed, but the former flakes are better for vivid visualizations of developed turbulence. For PIV, we use nylon powders, whose mean diameter and density are 50 $\mu$m and 1.03 g/cm$^3$, respectively.

### C. Working fluids

We examine three kinds of working fluids: water, a dilute solution of cationic surfactant, and a dilute solution of polymers. For the surfactant solution, we use cetyltrimethyl ammonium chloride (CTAC, the molecular weight 320.00) with counterions, sodium salicylate (NaSal, the molecular

weight 160.10). For the polymer solution, we use polyethylene oxide (PEO, the mean molecular weight 4 000 000). The solutions of both of CTAC and PEO are viscoelastic fluids, and, even when the concentration is very dilute, they can lead to significant turbulence reduction [53,55,61]. The additives are dissolved in water, and then the solutions are injected into the spherical cavity filled with degassed tap water. The concentrations of the CTAC and NaSal are 50 ppm by mass concentration; i.e., the molar ratio of the CTAC and NaSal is 1:2. The concentration of PEO solution is also set at 50 ppm. The solutions are so dilute that we may assume that the zero-shear viscosity of the solutions are the same as that of water. We therefore estimate Re for the solutions by using the value of the kinematic viscosity of water at the same temperature.

As mentioned in Sec. I, a key parameter of viscoelastic fluids is its characteristic time, $\tau$. It is not straightforward to define the characteristic time, $\tau$, of viscoelastic fluids because their rheological properties are generally complex and only partly known. One candidate is the relaxation time, $\tau = \eta/G$. Here $\eta$ and $G$ are the viscosity and elastic modulus of a working fluid, respectively. The rheological properties of the CTAC and PEO solutions have been extensively investigated, although measurements of the rheological properties of dilute solutions are not necessarily easy, and it is known that the relaxation time of these solutions is significantly different. For the CTAC solution with concentration 75 ppm, $\tau = O(0.1)$ s [62], whereas for the PEO solution with concentration 400 ppm, $\tau = O(10^{-3})$ s [63], which is the same order with Zimm's relaxation time [64] of PEO. We estimate the relaxation time of the PEO solution of 50 ppm is $\tau = O(10^{-3})$ s because Zimm's estimation holds for the dilute limit. As will be shown in Sec. III, the difference in the characteristic times of the CTAC and PEO solutions has a great effect on the onset of turbulence modification.

It is also known (see, e.g., Ref. [65,66]) that dilute CTAC solutions show the significant increase of the shear viscosity around the shear rate $\dot{\gamma} \approx 10\ \mathrm{s}^{-1}$ due to the so-called shear-induced structures. The drastic increase of the viscosity is observed in experiments where $\dot{\gamma}$ is either increased or decreased around $\dot{\gamma} \approx 10\ \mathrm{s}^{-1}$ (see the schematics shown in Fig. 10 below). Of importance is that the characteristic time, 0.1 s, of the non-Newtonian viscosity of CTAC solutions is in the same order with the relaxation time. We may therefore assume that the characteristic time of the viscoelasticity of the dilute CTAC solutions is about 0.1 s. Incidentally, such a non-Newtonian viscosity is not observed in dilute PEO solutions in the range that $10\ \mathrm{s}^{-1} \lesssim \dot{\gamma} \lesssim 1000\ \mathrm{s}^{-1}$ [67].

## III. RESULTS

As mentioned in Sec. I, our previous experiments [50] showed that the most developed turbulence of water in a precessing sphere is sustained at $\mathrm{Po} \approx 0.1$ when the Reynolds number is sufficiently high ($\mathrm{Re} \gtrsim 5000$). For weaker precession ($\mathrm{Po} \lesssim 0.02$), turbulence is dominated by a simple swirling motion about the spin axis. On the other hand, for stronger precession ($\mathrm{Po} \gtrsim 0.2$), a columnar quiescent region emerges along the precession axis. Thus, in the following, we focus on the turbulence for $\mathrm{Po} = 0.1$, since the purpose of the present study is to understand the sustaining mechanism of fully developed turbulence in a precessing sphere. We briefly show results for other values of Po in the Appendix.

### A. Overall observations by flow visualizations

Figure 4 shows the snapshots of the visualization using reflective flakes of turbulence of (a) water, (b) the CTAC solution, and (c) the PEO solution. The control parameters are common: $\mathrm{Re} = 8.02 \times 10^4$ and $\mathrm{Po} = 0.1$.

For water [Fig. 4(a)], fully developed turbulence is sustained in the entire region of the sphere. It is our purpose to understand the sustaining mechanism of this developed turbulence of water. Looking at the fluid motion in this visualization (see also the movie in the Supplemental Materials [68]), we may have a strong impression that small-scale eddies are created in the vicinity of the wall and advected into the bulk by large-scale swirling motions observed in the right-upper and left-bottom regions of these figures. These swirling motions are the cross sections of the pair of large-scale vortex tubes shown in Fig. 2. However, we will show in Sec. IV that this picture of

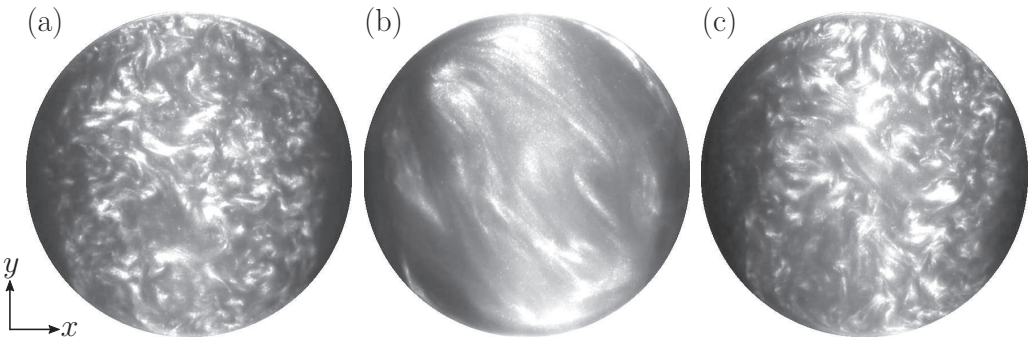


FIG. 4. Visualization with using aluminum flakes of turbulence for $\mathrm{Re} = 8.02 \times 10^4$ and $\mathrm{Po} = 0.1$. (a) Water, (b) CTAC solution (50 ppm), and (c) PEO solution (50 ppm). Movies are available in the Supplemental Materials [68].

turbulence sustainment is inaccurate and another mechanism is relevant to sustaining the small-scale turbulent eddies.

Despite the common Re and Po, the turbulence of the CTAC solution [Fig. 4(b)] is significantly weaker than that of water. More precisely, small-scale turbulent eddies, which exist in a central region in the water turbulence, almost completely disappear. Interestingly, however, looking at the fluid motion of the CTAC solution, we notice that large-scale swirling motions near the wall survive (see the movie in the Supplemental Materials [68]). We will show quantitative evidence of these observations in Secs. III B and III C.

In contrast to the case of the CTAC solution, no turbulence reduction is observed for the PEO solution [Fig. 4(c)]. Although this might be a surprising result because PEO is an additive frequently used to reduce turbulence intensity, it is explained in terms of the time-scale mismatch (Sec. IV). It is worth mentioning that even with much higher concentrations (up to 500 ppm) PEO solutions lead to no turbulence modification in the present experimental setup. Incidentally, since the turbulence for $\mathrm{Po} = 0.1$ is not accompanied by a simple global circulation (see Fig. 2) and well mixes additives [51] without centrifugal effects, the polymers uniformly distribute in the container. This implies that the absence of the turbulence reduction is not due to the accumulation of the polymers near the wall.

The above results are qualitatively similar (see Sec. III D for quantitative arguments) for the other Reynolds numbers: $\mathrm{Re} = 1.01 \times 10^4, 2.03 \times 10^4$, and $4.01 \times 10^4$. Irrespective of Re in this range, small-scale turbulent eddies in a central region of the sphere are drastically reduced for the dilute CTAC solution, whereas no turbulence modification is observed for the dilute PEO solution.

We emphasize that the flow states are quite robust in our experiments. This is in contrast to the known fact that the measurements of the rheological properties of these dilute solutions are difficult because they sometimes depend on measurement procedures. The high reproducibility of our experiments may be because we use a sufficiently large amount of the fluid (about $3.1 \times 10^3\ \mathrm{cm}^3$) and because we conduct the experiments according to a prescribed protocol with the precise control of the parameters. We always start with a solid-body rotational flow, i.e., without precession, at a given $\boldsymbol{\Omega}_s$ and suddenly impose the precession, and then wait for a sufficiently long time about 100 $T_s$ for the system to attain a statistically stationary state.

### B. Small-scale eddies

To quantitatively verify the observed feature of the reduction of small-scale turbulent eddies, we calculate the $z$ component, $\omega_z$, of the vorticity (the component in the direction perpendicular to the equatorial plane) by taking the spatial derivatives of the velocity fields obtained by using PIV. We evaluate the velocity gradients by the second-order finite difference. Figure 5 shows the instantaneous value of $\omega_z/\Omega_s$ in the semicircle region, $y \gtrsim 0$, on the equatorial plane. The parameters, Re and

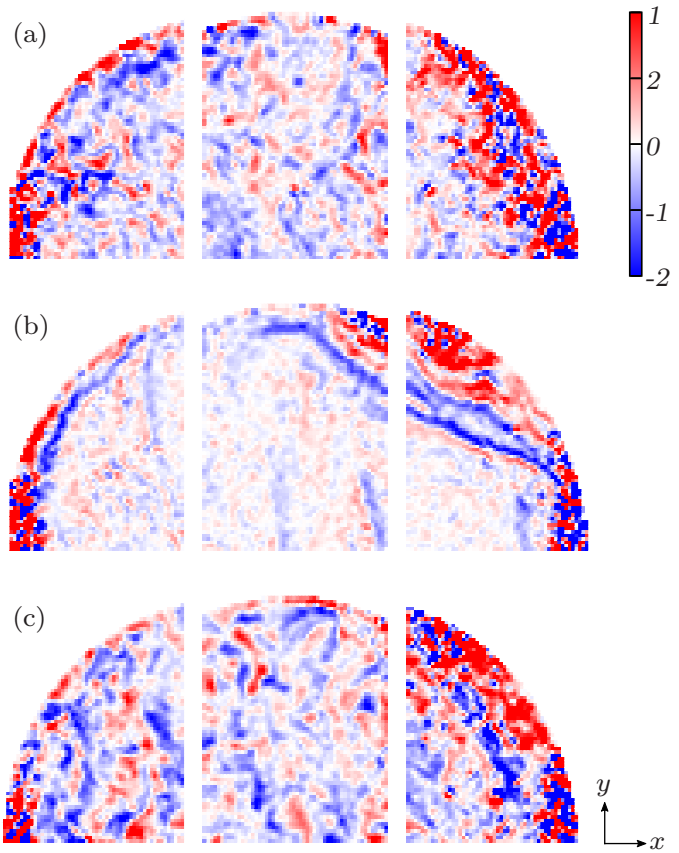


FIG. 5. Snapshots of the $z$-component vorticity, $\omega_z$, normalized by $\Omega_s$ for $\mathrm{Re} = 8.02 \times 10^4$ and $\mathrm{Po} = 0.1$. (a) Water, (b) CTAC solution (50 ppm), and (c) PEO solution (50 ppm). The left, center, and right columns show the regions that $-1 \leqslant x \lesssim -0.2$, $-0.4 \lesssim x \lesssim 0.4$, and $-0.2 \lesssim x \leqslant 1$, respectively.

Po, are the same as those in Fig. 4. Note that the results shown in Fig. 5 are vorticity fields at different times because we separately measure the velocity fields at three different locations in the $x$ direction (see Sec. II B). It is apparent, comparing Figs. 5(a) and 5(b), that small-scale eddies in a central region of the sphere are absent in turbulence of the CTAC solution. In contrast, there is no qualitative difference between small-scale turbulent eddies for water [Fig. 5(a)] and for the PEO solution [Fig. 5(c)]. These results are consistent with the flow visualizations shown in the previous subsection. Since we use different kinds of tracers for the visualizations and PIV (see Sec. II B), the turbulence modification and unmodification due to CTAC and PEO are not artifacts caused by the interactions between the reflective flakes and the additives.

To clarify the statistics of the reduction of turbulent eddies due to the additives, we plot in Fig. 6 the temporally averaged value of $(\omega_z/\Omega_s)^2$ for the three kinds of fluids. Since the value of $\omega_z$ reflects small-scale turbulent eddies and the positive-definite quantity $(\omega_z/\Omega_s)^2$ is not canceled out by the averaging, we can see in Fig. 6 how much the small-scale turbulence is reduced. The comparison between the three panels in Fig. 6 verifies that small-scale turbulent eddies are suppressed in the CTAC solution in a central region of the sphere, whereas no suppression occurs in the PEO solution. It is also clear in the comparison between Figs. 5(a) and 5(b) that the vorticity field near the wall is not modified even when small-scale turbulent eddies are drastically suppressed in the bulk of the flow of the CTAC solution.

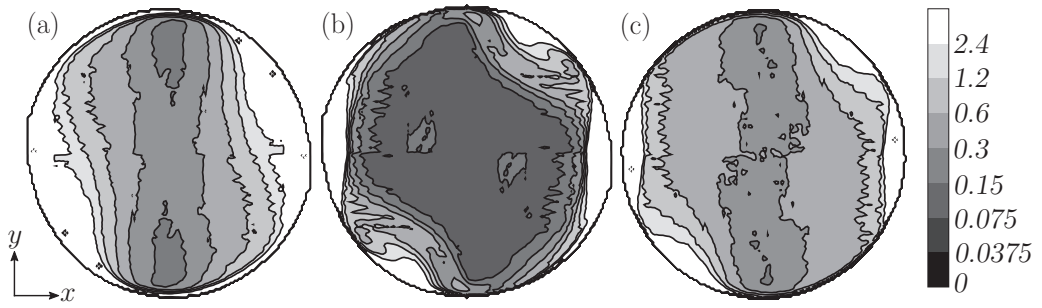


FIG. 6. Temporal average of $(\omega_z/\Omega_s)^2$ for $\mathrm{Re} = 8.02 \times 10^4$ and $\mathrm{Po} = 0.1$. (a) Water, (b) CTAC solution (50 ppm), and (c) PEO solution (50 ppm).

In the above discussion, we showed only the case for the highest Reynolds number, $\mathrm{Re} = 8.02 \times 10^4$, but the other cases are discussed in Sec. III D.

### C. Large-scale eddies

The supplemental movie for Fig. 4(b) cited Sec. III A suggests that although small-scale eddies are drastically reduced in the turbulence of the CTAC solution, the large-scale swirling motions survive. To quantitatively verify this feature of turbulence modification, we plot in Fig. 7 temporally averaged velocity fields, which represent large-scale flow structures, of turbulence of the three kinds of working fluids. Recall that we do not subtract the spin velocity of the container in Fig. 7. In these figures, the wall velocity is indicated by the vertical arrow, and we notice that the velocity in the bulk of the turbulence is, irrespective of the working fluid, much slower than the wall velocity.

In the turbulence of water [Fig. 7(a)], there are the large-scale swirling motions near the wall in the right-upper and left-bottom regions and counterflow in a central region. Recall that these near-wall structures are cross sections of a pair of large-scale vortex tubes (Fig. 2; see also Refs. [50] and [51]). In Fig. 2 we depict the mean flow structures on the basis of the DNS data of a Newtonian fluid. Although these vortices have only a small cross section with the equatorial plane, they induce counterclockwise vortices (Fig. 7) as shown by red curves in Fig. 7(b).

Comparing the temporally averaged velocity fields of turbulence of water [Fig. 7(a)] and the CTAC solution [Fig. 7(b)], we confirm that the large-scale swirling motions in the right-upper and left-bottom regions exist in the turbulence of the CTAC solution even when small-scale turbulent eddies are significantly reduced. We also notice that the size of the large-scale swirling motions in

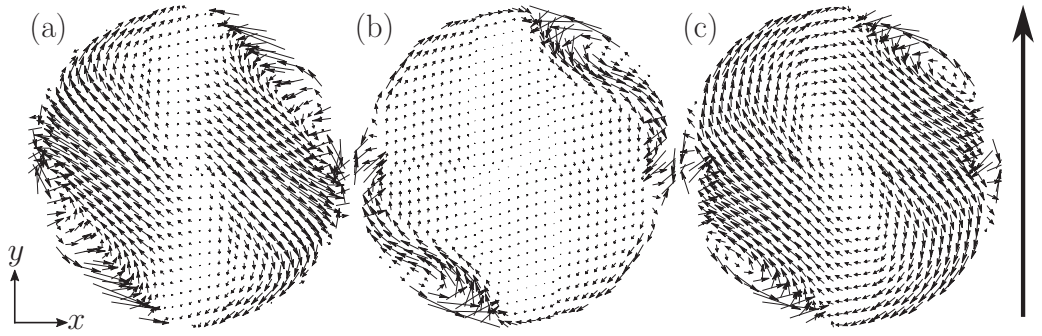


FIG. 7. Temporally averaged velocity field on the equatorial plane for $\mathrm{Re} = 8.02 \times 10^4$ and $\mathrm{Po} = 0.1$. (a) Water, (b) CTAC solution (50 ppm), and (c) PEO solution (50 ppm). The vertical thick arrow indicates the wall speed, $a\Omega_s$, on the equatorial plane. The direction of the spin of the container is counterclockwise.

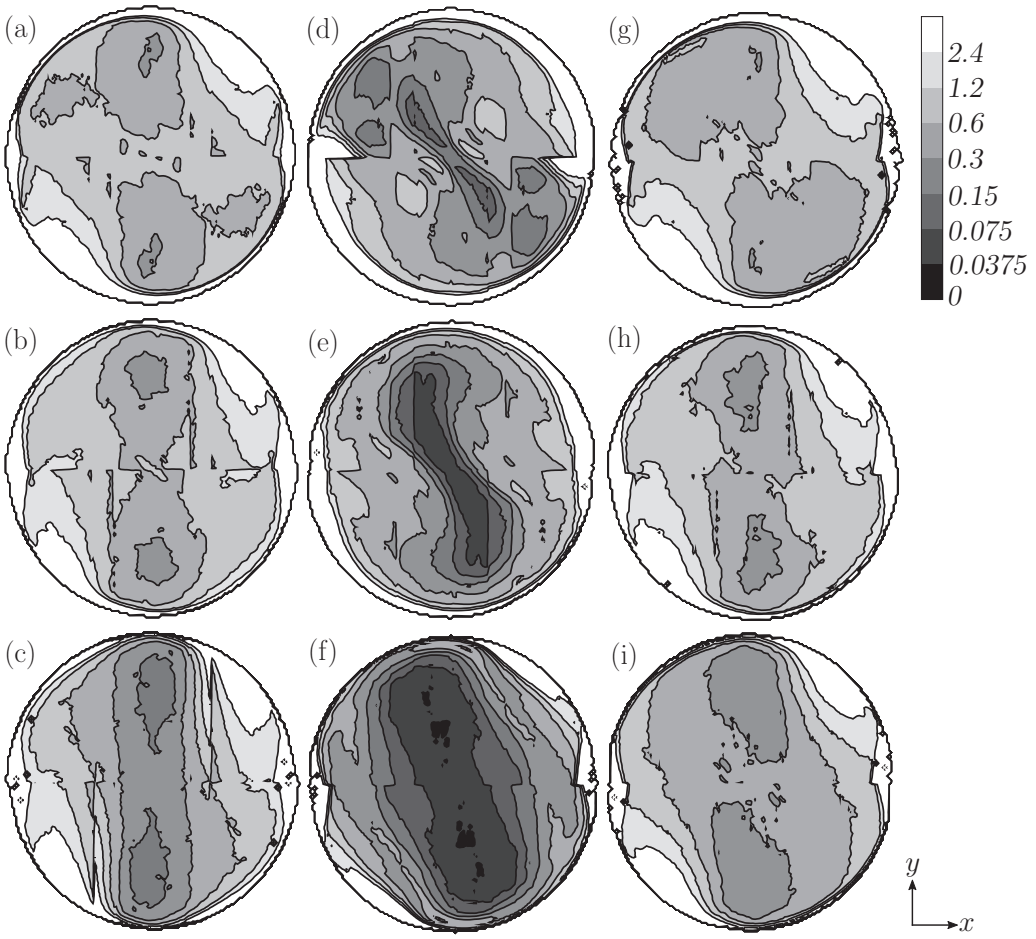


FIG. 8. Reynolds-number dependence of the temporally averaged value of $(\omega_z/\Omega_s)^2$ for Po = 0.1. (a, d, g) Re = $1.01 \times 10^4$, (b, e, h) $2.03 \times 10^4$, and (c, f, i) $4.01 \times 10^4$. (a–c) Water, (d–f) CTAC solution (50 ppm), and (g–i) PEO solution (50 ppm).

the CTAC solution at this Reynolds number (Re = $8.02 \times 10^4$) is smaller than in the turbulence of water. In other words, in the case shown in Fig. 7(b), although the large-scale swirling motions survive, they are modified by the CTAC additive, in particular, in their peripheries. The modification of large-scale eddies is examined in the next subsection in detail.

Incidentally, perhaps as expected from the observations in the previous subsections, the mean flow structures of turbulence of the water and PEO solution are almost identical [Figs. 7(a) and 7(c)]. The results shown in this and the preceding subsections imply that the PEO additive has no effect on structures of turbulence at any length scale in our system.

### D. Reynolds-number dependence of turbulence modification

Before closing this section, we investigate the Reynolds-number dependence of turbulence modification. This gives the key to the discussion in the next section. First, to examine the modification of small-scale turbulent eddies, we plot in Fig. 8 the temporally average of $(\omega_z/\Omega_s)^2$ of turbulence of the three working fluids at three different values of the Reynolds number (Re = $1.01 \times 10^4$, $2.03 \times 10^4$, and $4.01 \times 10^4$); see Fig. 6 for the results of Re = $8.02 \times 10^4$.

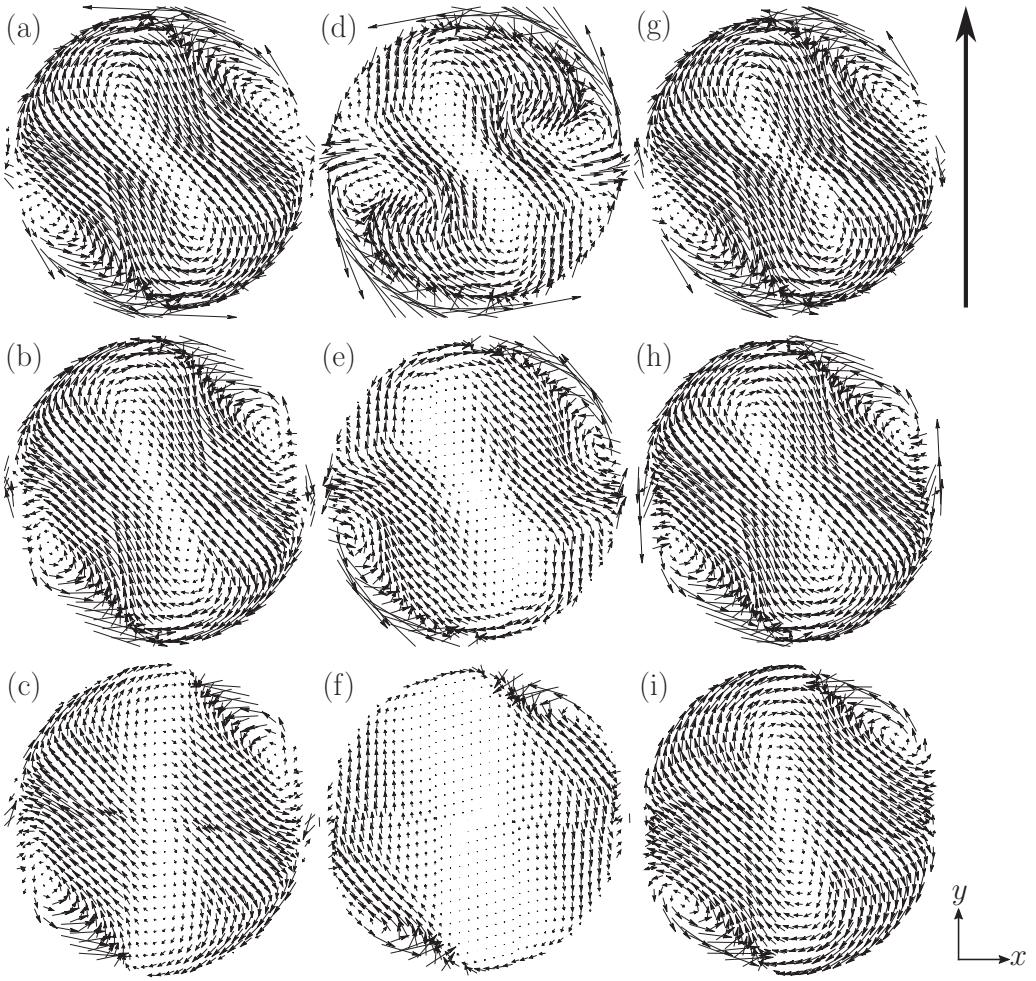


FIG. 9. Reynolds-number dependence of the temporally averaged velocity fields for Po = 0.1. (a, d, g) Re = $1.01 \times 10^4$, (b, e, h) $2.03 \times 10^4$, and (c, f, i) $4.01 \times 10^4$. (a–c) Water, (d–f) CTAC solution (50 ppm), and (g–i) PEO solution (50 ppm). The vertical thick arrow indicates the wall speed, $a\Omega_s$, on the equatorial plane. The direction of the spin of the container is counterclockwise.

Figures 6 and 8 show that, irrespective of Re, small-scale eddies are reduced in the bulk of the flow of the CTAC solution, whereas no modification of these small-scale eddies occurs in the PEO solution. Comparing the intensity of vorticity in water [Figs. 6(a) and 8(a)–8(c)] and the CTAC solution [Figs. 6(b) and 8(d)–8(f)], we see that the region of the turbulence reduction gradually expands as Re increases. More precisely, for the lowest Re [$=1.01 \times 10^4$; Fig. 8(d)] the reduction of small-scale turbulent eddies occurs only in a central region of the sphere, but small-scale eddies entirely disappear in the bulk of the sphere for the highest Re[$=8.02 \times 10^4$; Fig. 6(b)].

Next, to examine the modification of the large-scale flow, we show in Fig. 9 the temporally averaged velocity fields for the three Reynolds numbers (Re = $1.01 \times 10^4$, $2.03 \times 10^4$, and $4.01 \times 10^4$); the results for Re = $8.02 \times 10^4$ are shown in Fig. 7. Again, the PEO solution [Figs. 9(g)–9(i)] leads to no modification of large-scale flow at any Reynolds number. The comparison between the mean flow of the turbulence of water [Figs. 9(a)–9(c)] and the CTAC solution [Figs. 9(d)–9(f)] shows that, in the examined range of Re, the large-scale swirling motions in the right-upper and left-bottom regions on the equatorial plane always survive [Figs. 7(b) and 9(d)–9(f)]. Recall that these swirling

motions are the cross sections of a pair of large-scale vortex tubes (Fig. 2). However, looking at four panels in Figs. 7(b) and 9(d)–9(f), we notice that the large-scale vortices are also reduced for higher Re in their peripheries.

The summary of the Reynolds-number dependence of the turbulence modification due to the CTAC additive is as follows. (1) When the Reynolds number is as low as $1.01 \times 10^4$, turbulence reduction occurs only in small scales in a central region of the sphere. (2) The large-scale vortices (Fig. 2) survive even when small-scale turbulent eddies are reduced. (3) As Re increases, the intensity of the large-scale vortices is also reduced from their peripheries, and, for the highest Reynolds number ($\mathrm{Re} = 8.02 \times 10^4$; Fig. 7), the mean flow is modified in the almost entire region except for the near-wall structures observed in the right-upper and left-bottom regions on the equatorial plane. In other words, at the highest Reynolds number, only the largest eddies (Fig. 2), which become thinner than those in turbulence of water, survive, and no other scale motions exist in the sphere [see Fig. 4(b) and the movie in the Supplemental Materials [68]].

## IV. DISCUSSION: SUSTAINING MECHANISM OF THE TURBULENCE

We are ready to discuss the sustaining mechanism of the small-scale turbulent eddies of a Newtonian fluid in the precessing sphere. There are two possibilities of the sustaining mechanism. The first is that continuous advection of small-scale eddies generated in the vicinity of the wall sustains the turbulence. This advection might be caused by the pair of large-scale vortex tubes (Fig. 2). The second is that the small-scale turbulent eddies are sustained through an energy cascading process due to vortex stretching in shear flows around these large-scale vortices.

In fact, the former mechanism is irrelevant because it conflicts with our experimental results, although the naive observation of the flow visualization [Fig. 4(a) and the movie in the Supplemental Materials [68]] may suggest it. (Since the swirling motion around the pair of the large-scale vortex tubes is conspicuous in the visualization, one may have the impression that small-scale eddies are erupted from the thin boundary layer on the wall.) As shown in Secs. III C and III D, however, even when the CTAC additive drastically suppresses small-scale turbulent eddies, there exists a pair of large-scale vortex tubes as in the turbulence of water. Furthermore, Figs. 5, 6, and 8 show that the vorticity, $\omega_z$, in the vicinity of the wall is not suppressed even in the CTAC solution. Hence, if the former mechanism were correct, small-scale turbulent eddies would be observed even in the turbulence of the CTAC solution.

The Reynolds-number dependence shown in Sec. III D also denies the former mechanism. This mechanism would explain the turbulence modification as follows: small-scale structures advected from the near-wall region were suppressed by the viscoelasticity of the fluid. Note here that, as depicted in the left schematic in Fig. 10(a), the surfactant solution has non-Newtonian viscosity, which is significantly large for the shear rate around $\dot{\gamma}^{-1} \approx 10\ \mathrm{s}^{-1}$ [65,66]. Since the time scales of the flow (i.e., the reciprocal, $\dot{\gamma}^{-1}$, of the shear rate) in the vicinity of the wall are much shorter than those in the bulk flow (which will be verified in Fig. 11 below), if the former mechanism were correct, the turbulence reduction would occur at the distance from the wall where $\dot{\gamma}^{-1}$ becomes comparable to the characteristic time of the viscoelasticity [Fig. 10(a)]. In our experiments, a higher value of $\mathrm{Re} = a^2\Omega_s/\nu$ corresponds to a larger value of $\Omega_s$ because we use the same container for all the experiments. In other words, for higher Re, the spin is faster and the time scale of the flow is shorter as indicated by the two curves in Fig. 10. Therefore, if the former mechanism were valid, the region where turbulence is reduced would shrink for higher Reynolds numbers [Fig. 10(a)]. This is obviously inconsistent with our observation of the Reynolds-number dependence shown in Sec. III D (Figs. 6 and 8).

In contrast, the latter mechanism provides a reasonable explanation of the experimental observations. We use the classical theories [57–60] of turbulence modification in viscoelastic fluids, which explain that the energy cascade in turbulence of the CTAC solution terminates at $\ell_c$ [Fig. 10(b-1)]. Recall that the elastic theory [59,60] predicts that $\ell_c$ is smaller than the Lumley scale, $\ell_L$, for which the time scale of turbulent eddies is comparable to the characteristic time, $\tau$, of

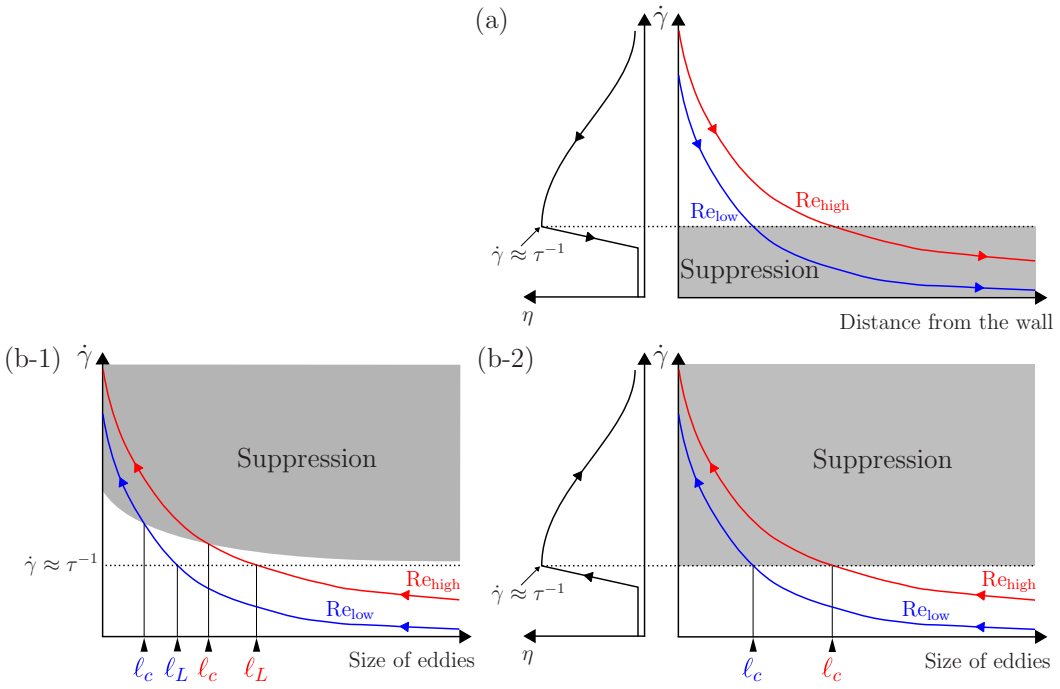


FIG. 10. Two possibilities of the Reynolds-number dependence of the turbulence modification. Right panels show the shear rate, $\dot{\gamma}$, as a function of (a) the distance from the wall and (b) the size of eddies for two different Reynolds numbers, $\mathrm{Re}_{\mathrm{low}} < \mathrm{Re}_{\mathrm{high}}$. (a) First possibility: small-scale turbulent eddies in a central region of the sphere are sustained by being advected from the wall. If this is the case, the region without the suppression of these eddies expands toward the center of the sphere as Re increases because the shear rate, $\dot{\gamma}$, of the flow gets smaller with the distance from the wall and the turbulence suppression occurs at the location where the time scale, $\dot{\gamma}^{-1}$, of the flow coincides with the characteristic time, $\tau$, of the fluid. The left panel depicting the viscosity, $\eta$, of the CTAC solution as a function of shear rate [65,66] shows that $\eta$ gets larger and takes a maximum value around $\dot{\gamma}^{-1} \approx \tau$. Note that $\dot{\gamma}$ at a given location is larger for higher Re in our experimental setup. (b) Second possibility in terms of (b-1) the elastic theory and (b-2) non-Newtonian viscosity: the turbulence is sustained by an energy cascading process in the bulk. If this is the case, only small eddies are reduced for lower Re, but larger ones are also reduced for higher Re because the suppression occurs at the length scale, $\ell_c$, which is larger for higher Re in our experiments. The precise meaning of the truncation scale, $\ell_c$, is different in (b-1) the elastic theory and in (b-2) the viscous theory, but this Reynolds-number dependence is common.

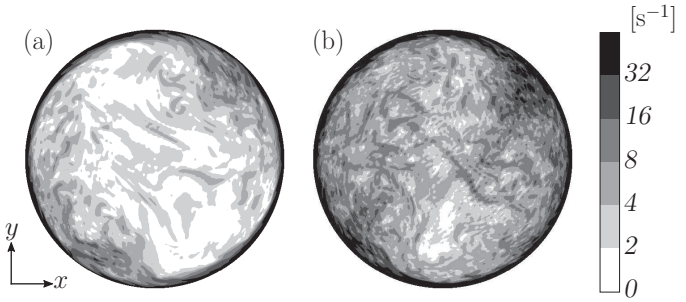


FIG. 11. Instantaneous profile of shear rate, $\dot{\gamma}$, of turbulence of a Newtonian fluid for $\mathrm{Po} = 0.1$. DNS results for our experimental setup ($a = 90$ mm and $\nu = 10^{-6}$ m$^2$/s). (a) $\mathrm{Re} = 1 \times 10^4$ and (b) $2 \times 10^4$. Contour levels are in a logarithmic scale. Recall that the reciprocal of the characteristic time of the CTAC solution is about 10 s$^{-1}$ (see Sec. II C).

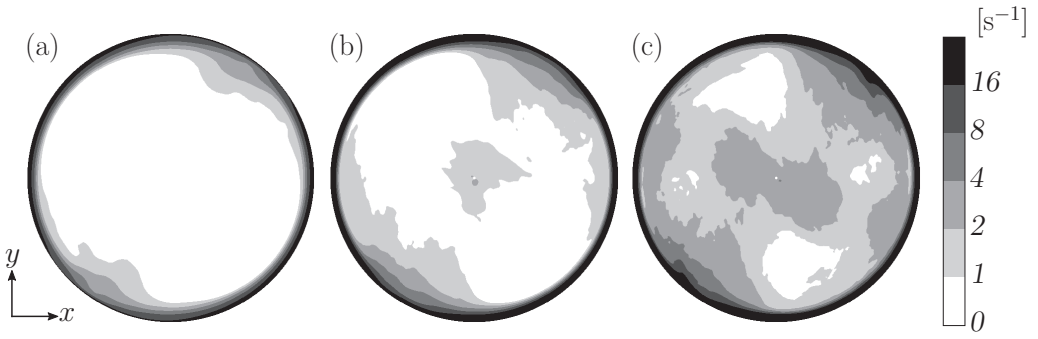


FIG. 12. Shear rate, $\dot{\Gamma}$, of temporally averaged velocity fields of turbulence of a Newtonian fluid for Po = 0.1. DNS results for our experimental setup ($a = 90$ mm and $\nu = 10^{-6}$ m$^2$/s). (a) Re $= 5 \times 10^3$, (b) $1 \times 10^4$, and (c) $2 \times 10^4$.

the fluid [Fig. 10(b-1)]. Then, the experimental results are explained as follows. Small-scale eddies are created through an energy cascade originating from the largest-scale eddies (Fig. 2) in turbulence of water, whereas, in turbulence of viscoelastic fluids, eddies smaller than $\ell_c$ are not created because the kinetic energy for such scales are transformed to the elastic energy. Incidentally, even if we consider only the non-Newtonian viscosity, instead of the elasticity, we can depict similar picture [Fig. 10(b-2)]. Namely, the length scale, $\ell_c$, where the viscosity significantly increases is determined by the time-scale matching, and the kinetic energy cannot be cascaded below $\ell_c$. It is important that these explanations are consistent with the observation that even when the large-scale vortices (Fig. 2) exist, small-scale eddies are drastically suppressed [Figs. 4(b) and 7(b)].

We verify in Fig. 11, by using DNS data, that the characteristic value of the shear rate, $\dot{\gamma}$, is indeed in the frequency range between $O(1)$ s$^{-1}$ and $O(10)$ s$^{-1}$ in the bulk of the turbulent flow at the Reynolds numbers examined in the present study. Here the shear rate, $\dot{\gamma}$, is evaluated by $\dot{\gamma} = \sqrt{\sum_{i,j=1}^{3} S_{ij} S_{ij}}$ with $S_{ij}$ being the rate-of-strain tensor,

$$S_{ij} = \frac{1}{2}\left(\frac{\partial u_i}{\partial x_j} + \frac{\partial u_j}{\partial x_i}\right), \tag{1}$$

of velocity field, $\boldsymbol{u}$. Note, in passing, that this range of the shear rate is consistent with the vorticity measured by using PIV; compare Figs. 8(b) and 11(b) with the value of $\Omega_s \approx 0.8\pi$ s$^{-1}$ for our experimental setup (the temperature of water is 20.0 °C and $a = 90$ mm). The relaxation time of the CTAC solution (about 0.1 s; see Sec. II C) does exist within the range. Incidentally, Fig. 11 also shows that the shear rate in the vicinity of the wall is much higher than 10 s$^{-1}$. This implies that the viscoelasticity of the CTAC solution does not affect the flow in the boundary layer near the wall.

Furthermore, the latter mechanism well explains the Reynolds-number dependence of the turbulence modification. Since, in our experimental setup, the time scale of the flow is shorter for higher Re, the length scale, $\ell_c$, at which the energy cascade terminates is larger for higher Re [Fig. 10(b)]. This is the reason why only small-scale eddies are affected for relatively small Re but even the largest-scale eddies are suppressed, in particular in their peripheries, for the two highest Reynolds numbers [Re $= 4.01 \times 10^4$ and $8.02 \times 10^4$; Figs. 7(b) and 9(f)]. To reinforce this conclusion, we show in Fig. 12 the profiles of shear rate,

$$\dot{\Gamma} = \sqrt{\sum_{i,j=1}^{3} \overline{S}_{ij} \overline{S}_{ij}}, \quad \overline{S}_{ij} = \frac{1}{2}\left(\frac{\partial \overline{u}_i}{\partial x_j} + \frac{\partial \overline{u}_j}{\partial x_i}\right), \tag{2}$$

of the temporally averaged velocity field, $\overline{\boldsymbol{u}}$, for Re $= 5 \times 10^3, 10^4$, and $2 \times 10^4$. Figure 12 shows that $\dot{\Gamma}$ in a central region becomes larger as Re increases, and the time-scale matching between $\dot{\Gamma}^{-1}$

and $\tau$ does not occur at low Reynolds numbers but does occur in the central region of the sphere at higher Reynolds numbers. This is indeed consistent with the Reynolds-number dependence of the modification of large-scale vortices in their peripheries shown in Sec. III D.

It is also worth mentioning that the above arguments in terms of the time-scale matching are consistent with the fact that no turbulence reduction occurs in the PEO solution. As described in Sec. II C, the time scales are $\tau = O(0.1)$ s for the CTAC solution and $\tau = O(10^{-3})$ s for the PEO solution. The time scales of the turbulent eddies in our system are much longer than the relaxation time of the PEO solution. We may need to use a smaller container, at similar Reynolds numbers, to observe turbulence modification with the PEO additive.

## V. CONCLUDING REMARKS

To understand the sustaining mechanism of developed turbulence of a Newtonian fluid confined in a precessing sphere, we have experimentally investigated the turbulence of water and two kinds of viscoelastic fluids (dilute solutions of surfactant, CTAC, and polymers, PEO). We choose the control parameters [$\mathrm{Re} = O(10^4)$ and $\mathrm{Po} = 0.1$] so that developed turbulence is sustained when the working fluid is water and investigate its modifications due to the additives. Our experimental observations are summarized as follows. (1) Small-scale turbulent eddies are suppressed in the CTAC solution, while no turbulence modification occurs in the PEO solution. (2) A pair of large-scale vortex tubes in turbulence (Fig. 2) exists, for $\mathrm{Po} = 0.1$, even when small-scale turbulent eddies are drastically suppressed in the CTAC solution. However, the large-scale vortex tubes are weakened, in their peripheries, by the CTAC additive when Re is high enough.

These experimental observations are consistently explained if we assume that small-scale turbulent eddies observed in the bulk of the water turbulence are sustained by an energy cascade originating from the large-scale vortices (Fig. 2). The naive speculation that small-scale eddies would be advected from the wall (see Fig. 4 and the movie in the Supplemental Materials [68]) is denied because it conflicts with the experimental results on the turbulence modification (Sec. IV). The detailed arguments on the physics of turbulence modification are beyond the scope of the present study, and we have employed the classical theories by Lumley [57,58] and Tabor and de Gennes [59]. These theories qualitatively explain all the experimental observations. First, recalling that the two kinds of examined viscoelastic fluids have quite different time scales of the viscoelasticity (Sec. II C), we see the reason why no turbulence modification at any length scale occurs for the PEO solution in our experiments. The relaxation time of the PEO solution [$O(10^{-3})$ s] [63] is much shorter than the time scales [$O(0.1)$–$O(1)$ s] of turbulence in the bulk under our experimental conditions (Fig. 11). Second, for the CTAC solution, the fact that turbulence suppression occurs from small scales corresponds to the interruption of energy cascade at $\ell_c$ [see Fig. 10(b)]. When the turbulence reduction occurs, the shear rate of the turbulence in our system is in a range between $O(1)$ $\mathrm{s}^{-1}$ and $O(10)$ $\mathrm{s}^{-1}$ (Figs. 11 and 12). Since the characteristic time of the CTAC solution is $O(0.1)$ s [62,65,66], the suppression of small-scale eddies is consistent with the mechanism explained in Sec. IV. Furthermore, because the time scales of the turbulence become shorter as Re increases, large-scale eddies are also affected by the CTAC additive when Re is high enough [Fig. 10(b)]. This is also consistent with the estimation of the shear rate of temporally averaged velocity field (Fig. 12).

It is worth mentioning that the viscoelasticity of working fluid may affect the turbulence transition of precession-driven flows. When we fix Re and increase Po from a sufficiently small value, the flow state changes to be steady, periodic and turbulent. In this transition regime for $\mathrm{Po} \lesssim 0.01$, the flow in a precessing sphere, even turbulent flow (see the Appendix for $\mathrm{Po} = 0.02$), globally rotates about an axis inclined from the spin axis of the container. As mentioned in Sec. I, the differential rotation between the container and the confined fluid plays an essential role in these globally rotating flows. More concretely, while Po increases, the differential rotation grows and the shear rate in the boundary layer near the wall becomes larger. This implies that, at a certain Poincaré number, the time scale of the boundary layer can be comparable with the characteristic time scale of the viscoelasticity of the fluid. Once this time-scale matching occurs, the transition process might be suppressed because the

differential rotation cannot become larger. It is therefore an interesting future experimental study to verify this inhibition of the transition by choosing experimental conditions so that the time-scale matching in the boundary layer occurs. It is also nontrivial whether or not the fully developed turbulence for Po $\approx 0.1$ is sustained even if such an inhabitation of transition occurs. Incidentally, it has been known that the developed turbulence in a precessing spheroid [5] and cylinder [69] appears through a subcritical transition.

Although turbulence modification caused by additives has been extensively investigated for many flows, its physical mechanism is not fully understood for each flow system, because the sustaining mechanism of turbulence itself is not fully understood. The understanding of wall-bounded turbulence is rapidly progressing by the help of extensive DNS studies. In addition to DNSs, experimental investigations of turbulence modification in wall-bounded turbulence may help us to reveal its sustaining mechanism. We emphasize that the present study cannot be achieved without the collaboration between the DNSs of flows of Newtonian fluids, which evaluate the shear-rate distribution in the sphere, and the laboratory experiments of the non-Newtonian fluids.

We also emphasize that the turbulence generator using the precession of a container is useful not only for table-top experiments but also for larger devices. For example, a large experimental device, whose cylindrical cavity for liquid sodium has 2 m diameter and the same height, is constructing for the purpose of a precession driven dynamo [70]. The present study has revealed the sustaining mechanism of turbulence in a precessing sphere, which implies that shear flow near the container's wall is not necessarily important for the sustainment of the turbulence. It is nontrivial large-scale vortices like those observed in our experiments (Fig. 2) that play essential roles in the sustainment of the turbulence in a precessing container. Hence, to drive fully developed turbulence by precession, one must choose experimental conditions so that large-scale vortices, which effectively create smaller-scale eddies, may be sustained. An important question remains, however: how are these nontrivial large-scale flow structures created by the weak precession of the container? Although a preliminary explanation was given in Ref. [36] on the basis of DNSs, we are conducting more detailed DNSs and will report the results elsewhere in the near future.

## ACKNOWLEDGMENTS

This study was partly supported by JSPS Grants-in-Aid for Scientific Research (24360071, 16H04268). The authors thank the anonymous referees for their constructive suggestions.

## APPENDIX: TURBULENCE MODIFICATION FOR OTHER Po

We show the experimental results for Po $= 0.1$ in the main text. In this Appendix, we briefly summarize results of flow visualizations for smaller and larger Poincaré numbers (Po $= 0.02$ and

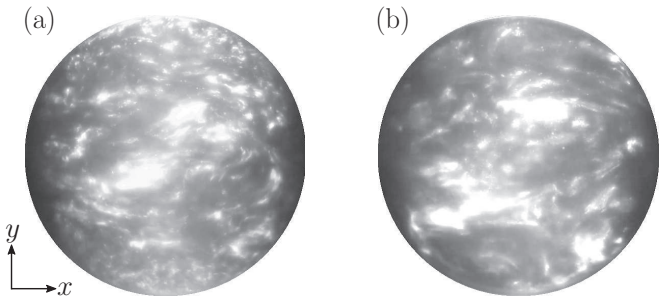


FIG. 13. Visualization with using mica flakes coated with titanium dioxide of turbulence for Po $= 0.02$ and Re $= 8.02 \times 10^4$. (a) Water and (b) CTAC solution (50 ppm). Movies are available in the Supplemental Materials [68].

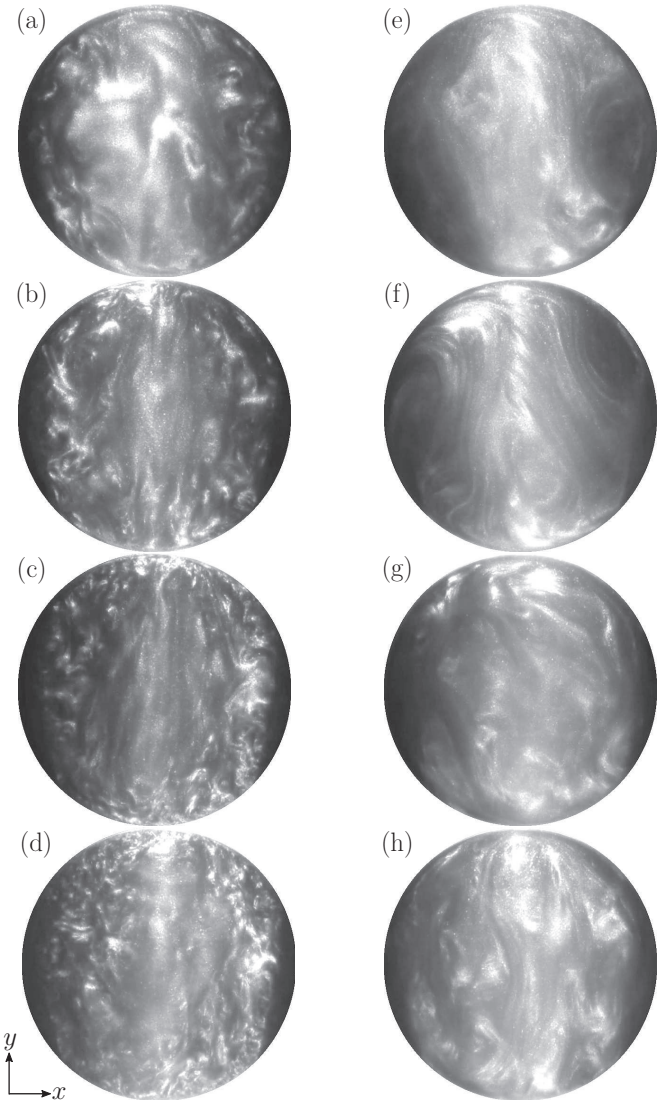


FIG. 14. Visualization with using aluminum flakes of turbulence for Po = 0.2. (a, e) Re = $1.01 \times 10^4$, (b, f) Re = $2.03 \times 10^4$, (c, g) $4.01 \times 10^4$, and (d, h) $8.02 \times 10^4$. (a–d) Water and (e–h) CTAC solution (50 ppm).

0.2). As expected from the time-scale arguments (see Sec. IV), we do not observe any qualitative difference between the turbulence of water and the PEO solution in the Reynolds-number range $10^4 \lesssim \mathrm{Re} \lesssim 8 \times 10^4$ in both cases of Po (figures are omitted). We compare results for water and the CTAC solution in Figs. 13 (Po = 0.02) and 14 (Po = 0.2).

For the smaller Poincaré number (Po = 0.02; Fig. 13), the spin dominates the precession, and the mean flow of the turbulence is a simple large-scale circulation about an axis inclined by little from the spin axis due to the Coriolis force. Therefore, the shear rates in the turbulence are smaller than the case with Po = 0.1. This is the reason why turbulence modification does not occur when Re is low (figures are omitted). When Re is higher (Re = $8.02 \times 10^4$), since the shear rate is large enough, we may observe suppression of small-scale turbulent eddies; see an upper region of Fig. 13(b) (the modification is clearer in the movie in the Supplemental Materials [68]). These observations are consistent with the arguments developed in the main text (Sec. IV).

Incidentally, as shown by the DNS [38,39], turbulence for low Po globally rotates about an axis tilted from the spin axis, and there exist coherent vortices, which are quasisteady in the frame rotating together with the fluid. These vortices are the essential elements of the turbulence, but we have to note that the present experimental setup, which measures velocity fields on the equatorial plane rather than the cross section of the fluid rotation, may not capture the vortices.

For the larger Poincaré number (Po = 0.2), we show snapshots of the flake visualization of the turbulence of water [Figs. 14(a)–14(d)] and the CTAC solution [Figs. 14(e)–14(f)]. The Reynolds numbers are Re = $1.01 \times 10^4$ [Figs. 14(a) and 14(e)], $2.03 \times 10^4$ [Figs. 14(b) and 14(f)], $4.01 \times 10^4$ [Figs. 14(c) and 14(g)], and $8.02 \times 10^4$ [Figs. 14(d) and 14(h)]. Since, in contrast to the spin axis, the precession axis is fixed in the laboratory frame, in this precession dominant case, the turbulent flow of a Newtonian fluid becomes quiescent in a columnar region along the precession axis, and small-scale turbulent eddies are sustained only outside the column; see the results for water in Figs. 14(a)–14(d). Similarly to the case of Po = 0.1, these small-scale turbulent eddies are reduced in the CTAC solution; and the reduction is clearer for higher Re because the shear rates are larger (see the arguments in Sec. IV).


[1] S. Douady, Y. Couder, and M. E. Brachet, Direct Observation of the Intermittency of Intense Vorticity Filaments in Turbulence, Phys. Rev. Lett. **67**, 983 (1991).

[2] O. Cadot, S. Douady, and Y. Couder, Characterization of the low-pressure filaments in a three-dimensional turbulent shear flow, Phys. Fluids **7**, 630 (1995).

[3] G. I. Taylor, Stability of a viscous liquid contained between two rotating cylinders, Phil. Trans. Roy. Soc. **223**, 289 (1923).

[4] S. Grossmann, D. Lohse, and C. Sun, High-Reynolds number Taylor-Couette turbulence, Ann. Rev. Fluid Mech. **48**, 53 (2016).

[5] W. V. R. Malkus, Precession of the earth as the cause of geomagnetism: Experiments lend support to the proposal that precessional torques drive the Earth's dynamo, Science **160**, 259 (1968).

[6] S. Goto, N. Ishii, S. Kida, and M. Nishioka, Turbulence generator using a precessing sphere, Phys. Fluids **19**, 061705 (2007).

[7] R. Manasseh, Breakdown regimes of inertia waves in a precessing cylinder, J. Fluid Mech. **243**, 261 (1992).

[8] R. Manasseh, Distortions of inertia waves in a rotating fluid cylinder forced near its fundamental mode resonance, J. Fluid Mech. **265**, 345 (1994).

[9] R. Manasseh, Nonlinear behaviour of contained inertia waves, J. Fluid Mech. **315**, 151 (1996).

[10] J. J. Kobine, Inertial wave dynamics in a rotating and precessing cylinder, J. Fluid Mech. **303**, 233 (1995).

[11] J. J. Kobine, Azimuthal flow associated with inertial wave resonance in a precessing cylinder, J. Fluid Mech. **319**, 387 (1996).

[12] P. Meunier, C. Eloy, R. Lagrange, and F. Nadal, A rotating fluid cylinder subject to weak precession, J. Fluid Mech. **599**, 405 (2008).

[13] R. Lagrange, C. Eloy, F. Nadal, and P. Meunier, Instability of a fluid inside a precessing cylinder, Phys. Fluids **20**, 081701 (2008).

[14] C. Nore, J. Léorat, J.-L. Guermond, and F. Luddens, Nonlinear dynamo action in a precessing cylindrical container, Phys. Rev. E **84**, 016317 (2011).

[15] C. Nore, D. C. Quiroz, J.-L. Guermond, J. Léorat, and F. Luddens, Numerical dynamo action in cylindrical containers, Eur. Phys. J. Appl. Phys. **70**, 31101 (2015).

[16] W. Mouhali, T. Lehner, J. Léorat, and R. Vitry, Evidence for a cyclonic regime in a precessing cylindrical container, Exp. Fluids **53**, 1693 (2012).

[17] L. Cappanera, J.-L. Guermond, J. Léorat, and C. Nore, Two spinning ways for precession dynamo, Phys. Rev. E **93**, 043113 (2016).

[18] R. R. Kerswell, Upper bounds on the energy dissipation in turbulent precession, J. Fluid Mech. **321**, 335 (1996).
[19] K. Stewartson and P. H. Roberts, On the motion of a liquid in a spheroidal cavity of a precessing rigid body, J. Fluid Mech. **17**, 1 (1963).
[20] P. H. Roberts and K. Stewartson, On the motion of a liquid in a spheroidal cavity of a precessing rigid body. II, Proc. Camb. Phil. Soc. **61**, 279 (1965).
[21] F. H. Busse, Steady fluid flow in a precessing spheroidal shell, J. Fluid Mech. **33**, 739 (1968).
[22] J. P. Vanyo, A geodynamo powered by luni-solar precession, Geophys. Astrophys. Fluid Dyn. **59**, 209 (1991).
[23] J. Vanyo, P. Wilde, P. Cardin, and P. Olson, Experiments on precessing flows in the Earth's liquid core, Geophys. J. Int. **121**, 136 (1995).
[24] J. P. Vanyo and J. R. Dunn, Core precession: flow structures and energy, Geophys. J. Int. **142**, 409 (2000).
[25] R. R. Kerswell, The instability of precession flow, Geophys. Astrophys. Fluid Dyn. **72**, 107 (1993).
[26] J. Noir, D. Brito, K. Aldridge, and P. Cardin, Experimental evidence of inertial waves in a precessing spheroidal cavity, Geophy. Res. Lett. **28**, 3785 (2001).
[27] J. Noir, P. Cardin, D. Jault, and J.-P. Masson, Experimental evidence of nonlinear resonance effects between retrograde precession and the tilt-over mode within a spheroid, Geophys. J. Int. **154**, 407 (2003).
[28] J. P. Vanyo and P. W. Likins, Measurement of energy dissipation in a liquid-filled, precessing, spherical cavity, J. Appl. Mech. **38**, 674 (1971).
[29] J. P. Vanyo, An energy assessment for liquids in a filled precessing spherical cavity, J. Appl. Mech. **40**, 851 (1973).
[30] J. Noir, D. Jault, and P. Cardin, Numerical study of the motions within a slowly precessing sphere at low Ekman number, J. Fluid Mech. **437**, 282 (2001).
[31] A. Tilgner, Precession driven dynamos, Phys. Fluids **17**, 034104 (2005).
[32] A. Tilgner, Kinematic dynamos with precession driven flow in a sphere, Geophys. Astrophys. Fluid Dyn. **101**, 1 (2007).
[33] S. Kida and M. Shimizu, A turbulent ring and dynamo in a precessing sphere, J. Phys.: Conf. Ser. **318**, 072031 (2011).
[34] S. Kida, Steady flow in a rapidly rotating sphere with weak precession, J. Fluid Mech. **680**, 150 (2011).
[35] S. Kida, Instability by weak precession of the flow in a rotating sphere, Procedia IUTAM **7**, 183 (2013).
[36] Y. Koike, M. Shimizu, S. Kida, G. Kawahara, and S. Goto, Continuous spin-up and dynamo in a precessing sphere, Proc. JSST 2012, 190 (2012).
[37] R. Hollerbach, C. Nore, P. Marti, S. Vantieghem, F. Luddens, and J. Léorat, Parity-breaking flows in precessing spherical containers, Phys. Rev. E **87**, 053020 (2013).
[38] Y. Lin, P. Marti, and J. Noir, Shear-driven parametric instability in a precessing sphere, Phys. Fluids **27**, 046601 (2015).
[39] Y. Lin, P. Marti, J. Noir, and A. Jackson, Precession-driven dynamos in a full sphere and the role of large scale cyclonic vortices, Phys. Fluids **28**, 066601 (2016).
[40] R. Hollerbach and R. R. Kerswell, Oscillatory internal shear layers in rotating and precessing flows, J. Fluid Mech. **298**, 327 (1995).
[41] R. R. Kerswell, On the internal shear layers spawned by the critical regions in oscillatory Ekman boundary layers, J. Fluid Mech. **298**, 311 (1995).
[42] A. Tilgner, Magnetohydrodynamics flow in precessing spherical shells, J. Fluid Mech. **379**, 303 (1999).
[43] A. Tilgner, Non-axisymmetric shear layers in precessing fluid ellipsoidal shells, Geophys. J. Int. **136**, 629 (1999).
[44] A. Tilgner and F. H. Busse, Fluid flows in precessing spherical shells, J. Fluid Mech. **426**, 387 (2001).
[45] S. Lorenzani and A. Tilgner, Fluid instabilities in precessing spheroidal cavities, J. Fluid Mech. **447**, 111 (2001).
[46] S. Lorenzani and A. Tilgner, Inertial instabilities of fluid flow in precessing spheroidal shells, J. Fluid Mech. **492**, 363 (2003).
[47] H. Bondi and R. A. Lyttleton, On the dynamical theory of the rotation of the earth. II. The effect of precession on the motion of the liquid core, Math. Proc. Camb. Phil. Soc. **49**, 498 (1953).

[48] C. C. Wu and P. H. Roberts, On a dynamo driven by topographic precession, Geophys. Astrophys. Fluid Dyn. **103**, 467 (2009).
[49] M. Le Bars, D. Cébron, and P. Le Gal, Flows driven by libration, precession, and tides, Ann. Rev. Fluid Mech. **47**, 163 (2015).
[50] S. Goto, A. Matsunaga, M. Fujiwara, M. Nishioka, S. Kida, M. Yamato, and S. Tsuda, Turbulence driven by precession in spherical and slightly elongated spheroidal cavities, Phys. Fluids **26**, 055107 (2014).
[51] S. Goto, M. Shimizu, and G. Kawahara, Turbulent mixing in a precessing sphere, Phys. Fluids **26**, 115106 (2014).
[52] N. S. Berman, Drag reduction by polymers, Ann. Rev. Fluid Mech. **10**, 47 (1978).
[53] J. L. Zakin, B. Lu, and H.-W. Bewersdorff, Surfactant drag reduction, Rev. Chem. Eng. **14**, 253 (1998).
[54] C. M. White and M. G. Mungal, Mechanics and prediction of turbulent drag reduction with polymer additives, Annu. Rev. Fluid Mech. **40**, 235 (2008).
[55] Y. Wang, B. Yu, J. L. Zakin, and H. Shi, Review on drag reduction and its heat transfer by additives, Adv. Mech. Eng. **3**, 478749 (2011).
[56] B. A. Toms, Some observation on the flow of linear polymer solutions through straight tubes at large Reynolds numbers, Proc. 1st Intl. Congr. on Rheology **2**, 135 (1948).
[57] J. L. Lumley, Drag reduction by additives, Annu. Rev. Fluid Mech. **1**, 367 (1969).
[58] J. L. Lumley, Drag reduction in turbulent flow by polymer additives, J. Polymer Sci.: Macromol. Rev. **7**, 263 (1973).
[59] M. Tabor and P. G. de Gennes, A cascade theory of drag reduction, Europhys. Lett. **2**, 519 (1986).
[60] P. G. de Gennes, *Introduction to Polymer Dynamics* (Cambridge University Press, Cambridge, 1990).
[61] S.-Q. Yang, Drag reduction in turbulent flow with polymer additives, J. Fluids Eng. **131**, 051301 (2009).
[62] B. Yu, F.-C. Li, and Y. Kawaguchi, Numerical and experimental investigation of turbulent characteristics in a drag-reducing flow with surfactant additives, Int. J. Heat and Fluid Flow **25**, 961 (2004).
[63] J. Zilz, C. Schäfer, C. Wagner, R. J. Poole, M. A. Alves, and A. Lindner, Serpentine channels: Micro-rheometers for fluid relaxation times, Lab Chip **14**, 351 (2014).
[64] B. H. Zimm, Dynamics of polymer molecules in dilute solution: Viscoelasticity, flow birefringence and dielectric loss, J. Chem. Phys. **24**, 269 (1956).
[65] H. Usui and K. Kimura, Drag reduction caused by cationic surfactants, Proc. PPS Int. Conf. Rheology and Polymer, 76 (1990).
[66] C.-H. Liu and D. J. Pine, Shear-Induced Gelation and Fracture in Micellar Solutions, Phys. Rev. Lett. **77**, 2121 (1996).
[67] I. Zadrazil, A. Bismarck, G. F. Hewitt, and C. N. Markides, Shear layers in the turbulent pipe flow of drag reducing polymer solutions, Chem. Eng. Sci. **72**, 142 (2012).
[68] See Supplemental Material at http://link.aps.org/supplemental/10.1103/PhysRevFluids.2.114603 for Figs. 4 and 13. For Fig. 4, movie4.mpeg shows turbulence of (upper) water and (lower) the CTAC solution (50 ppm) for $\mathrm{Po} = 0.1$ and $\mathrm{Re} = 8.02 \times 10^4$. For Fig. 13, movie13.mpeg shows the turbulence of (upper) water and (lower) the CTAC solution (50 ppm) for $\mathrm{Po} = 0.02$ and $\mathrm{Re} = 8.02 \times 10^4$.
[69] J. Herault, T. Gundrum, A. Giesecke, and F. Stefani, Subcritical transition to turbulence of a precessing flow in a cylindrical vessel, Phys. Fluids **27**, 124102 (2015).
[70] F. Stefani, T. Albrecht, G. Gerbeth, A. Giesecke, T. Gundrum, J. Herault, C. Nore, and C. Steglich, Towards a precession driven dynamo experiment, Magnetohydrodynamics **51**, 275 (2015).